

Thermal optimization of a totally enclosed forced ventilated permanent magnet traction motor using lumped parameter and partial computational fluid dynamics modeling*

Wei CHEN^{†1}, Gui-chu WU¹, You-tong FANG², Ji-en MA²

¹Key Laboratory of Low-Voltage Apparatus Intellectual Technology of Zhejiang,
Wenzhou University, Wenzhou 325027, China

²College of Electrical Engineering, Zhejiang University, Hangzhou 310027, China

[†]E-mail: chenwei1989@wzu.edu.cn

Received Dec. 1, 2017; Revision accepted June 5, 2018; Crosschecked Oct. 29, 2018

Abstract: In this study, we present a thermal optimization method using the overall lumped parameter (LP) and partial computational fluid dynamics (CFD) modeling for a 600-kW permanent magnet traction motor developed for high-speed trains. The motor is totally enclosed forced ventilated to achieve high power density, high efficiency, and low maintenance requirements. Considering the electro-magnetic performance, bogie space, and thermal capacity, we propose a ventilation structure with zigzag plates in sector cross-section. We focus particularly on the ventilation channels and propose an overall LP model for thermal optimization, in which the full consideration of the influence of turbulent flow is given by using a partial CFD model. Given the specific critical parameters from the optimization results, we present a complete 3D CFD model of the whole motor to obtain an accurate temperature distribution and the maximum temperature rises in local points. The benefit of zigzag plates is studied extensively using both the LP and the complete CFD models and the results are verified by equivalent thermal experiments under rated operations. Experimental results indicate that the ventilation structure fulfills the normal operational demands of high-speed trains by improving thermal performance by more than 15%. Additionally, we propose an engineering method to estimate iron loss constraint with the complete CFD model to guide the control system design.

Key words: Computational fluid dynamics (CFD); Lumped parameter (LP) model; Permanent magnet (PM) synchronous motors; Totally enclosed forced ventilated motor

<https://doi.org/10.1631/jzus.A1700649>

CLC number: TM301.4

1 Introduction

The annual electricity consumption of high-speed trains is extremely high, because of their heavy loads and long working hours. Therefore, perma-

nent magnet (PM) motors are particularly suitable for high-speed trains owing to their superior power density and efficiency, low noise, and low maintenance costs (Mademlis et al., 2004; El-Refaie et al., 2006; Mizuno et al., 2013; Huang et al., 2015; Hao et al., 2016). Over the last decades, the application of PM motors in rail vehicles has been extensive (e.g. in France, Japan, Germany, and Canada). For high-speed trains, PM motors with a totally enclosed self-cooling structure were first put into commercial operation on automatic guided vehicle (AGV) Italo

* Project supported by the National Natural Science Foundation of China (Nos. 51607123, 51577166, and U1434202) and the Fund of Wenzhou Municipal Science and Technology Bureau, China (No. ZG2017002)

 ORCID: Wei CHEN, <https://orcid.org/0000-0002-6915-8979>

© Zhejiang University and Springer-Verlag GmbH Germany, part of Springer Nature 2018

trains by the French company Alstom (Feng, 2012).

In this study, we develop a 600-kW PM traction motor (power density up to 1 kW/kg) for Chinese high-speed rail trains. However, high-speed trains push the electro-magnetic performance of traction motors to the extreme. Winding insulation and PM materials are subjected to certain temperature limits, and thermal management becomes one of the major challenges for designers. Compared to the motors on AGV Italo, challenges are posed to electro-magnetic and thermal design to reach the same power density level with the smaller space of CRH380A bogies. To achieve a low maintenance cost and a long working life, a totally enclosed forced ventilation (TEFV) structure is introduced to protect PMs from dust and iron filings.

Ventilation design of traction motors needs to strike a balance between electro-magnetic and thermal performances. A good electro-magnetic design will lead to a high power density while a good thermal design will be able to transfer losses to external surfaces. The latter ensures that the temperatures of winding and magnets do not surpass the insulation temperature limit and Curie point, respectively. Given the space of the CRH380A bogie and specific ventilation conditions (supplied by the train system), we evaluate the thermal behavior of the motor in the preliminary design and optimize ventilation channels using a lumped parameter (LP) model assisted by a partial computational fluid dynamics (CFD) model (Jungreuthmayer et al., 2011; Nategh et al., 2013; Tan et al., 2015; Qian et al., 2016; He et al., 2017).

In the process of electro-magnetic design, the geometric data of the permanent magnet motor are specified. With these data and material properties, the thermal parameters of the motor components can be computed. The LP model is introduced to the preliminary design and optimization of ventilation channels because of its low computing requirements with an acceptable accuracy for steady and transient analysis (Boglietti and Cavagnino, 2007; Kral et al., 2008; Huang et al., 2009). In this model, heat sources are computed by the electro-magnetic finite element analysis (FEA). Normally, LP models are built by dividing motors into finite control volumes with thermal resistances and heat sources. In this TEFV motor, the important resistances between the stator and the housing determine the cooling performance of the ventilation channels. In the pro-

cess of ventilation channel optimization, the particular coolant flow conditions are not explicitly known. Therefore, the CFD method is applied and a partial CFD model of the ventilation channels is built to simulate the flow condition and compute convection coefficients for optimization (Ji et al., 2017).

CFD is based on the solution to the Reynolds-averaged Navier-Stokes (RANS) equations, covering the transfer of impulse conservation of mass and energy, as well as the transfer of turbulence energy (Wesseling, 2001; Kral et al., 2009). By taking the flow state and energy into consideration, CFD can help determine convection coefficients, as well as predict the temperature distribution. The advantage of CFD over the LP model is not only the inherent consideration of the coolant flows and the actual heat transfer coefficients, but also the results of a 3D temperature distribution. This temperature distribution makes a contribution in indicating the maximum temperature points, which may lead to a local failure of insulation or PM materials. Because of the high computational effort (Kral et al., 2009) and complexity of overall 3D modeling, especially the manual fine mesh generation, the CFD method is more attractive for precise flow and temperature simulation than thermal optimization.

In this study, zigzag plates, which bring a larger coolant interface area as well as a more complex flow condition, are introduced to the ventilation channels. To determine the critical parameters, the advantages of both LP and CFD modeling are exploited. Particularly, an overall LP model coupled with a partial CFD model is built for thermal analysis and optimization. The partial CFD model is used to simulate the turbulent flow condition and to calculate convection coefficients inside ventilation channels. According to the calculated coefficients, input parameters of thermal resistances for the overall LP model are provided. Considering the thermal influence on the flow condition, convection coefficients are re-calculated by importing results of heat flow from the overall LP model into the partial CFD model. Thus, the structure is finally settled and an overall CFD model is built to acquire temperature distribution as well as local points of the maximum temperature rise. Simulation results are verified by experimental tests under a rated operation and the benefits of zigzag plates are discussed. Moreover, the iron loss constraint is predicted by the proposed CFD model.

2 Optimization via the overall lumped parameter and partial computational fluid dynamics model

2.1 Original thermal design

A ventilation structure is built not only to ensure the normal operation of traction systems, but also to leave enough safety for long-life operation for high-speed railway applications. In this TEFV motor, fluid areas are divided into two parts, including air coolant and inner air (Fig. 1). The air coolant is pumped into the front end-cap and pressed through ventilation channels between the housing and the stator, illustrated by the red line. Assisted by the fan, inner air makes a contribution in enhancing convective heat transfer from end-winding to end-cap as well as in reducing temperature difference between rear and front components.

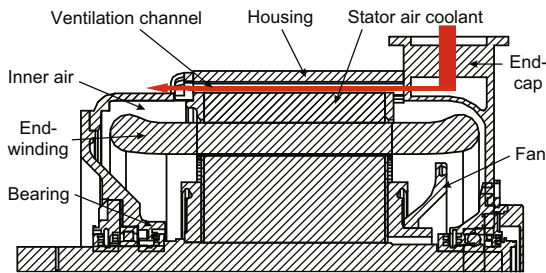


Fig. 1 Sketch of the totally enclosed forced ventilation motor and air coolant path. References to color refer to the online version of this figure

Fig. 2 and Table 1 present the geometry and general data of the TEFV PM motor, respectively. Zigzag plates are marked in red in ventilation channels and critical parameters are pointed out. Working from the thermal design experience of motors at the same level of power and power density from the company South China South Railway (merged into CRRC Corporation Limited in 2015), the number of ventilation channels was determined as 16 with an angle of 22.5° for each. Tests of the zigzag plate design were carried out as follows: (1) Only two included angles of adjacent branches were assigned, defined as θ_1 and θ_2 (Fig. 2); (2) All branches were designed to be of the same length, which makes the two angles exclusive when the number of the branches was determined. Table 2 presents three selected controllable parameters and their levels.

Since the inlet air coolant is supplied by the ventilation system on carriages, the flow condition is

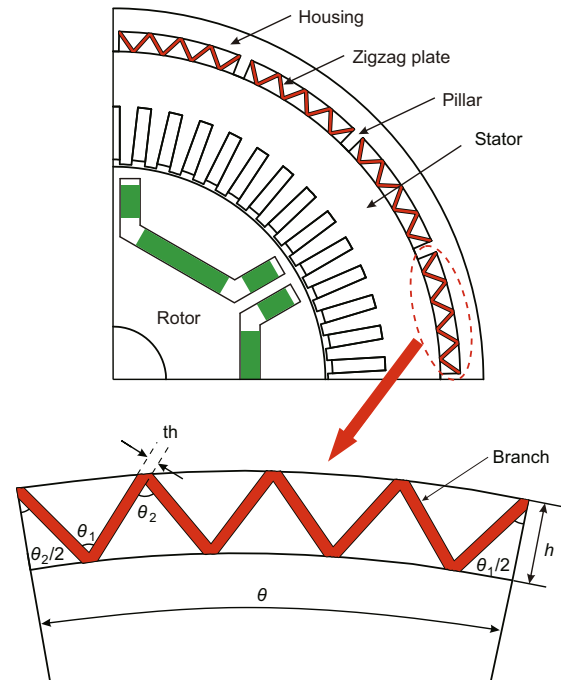


Fig. 2 Design of ventilation channels and parameters. References to color refer to the online version of this figure

Table 1 Data of the totally enclosed forced ventilation motor

Parameter	Description
Rated power (kW)	600
Rated speed (r/min)	4200
Stator outer diameter (mm)	500
Rotor outer diameter (mm)	316
Air-gap length (mm)	2
Stack length (mm)	260
Magnet segment thickness (mm)	16
Shaft diameter (mm)	80
Number of slots/poles	54/6
Number of strands per coil	8
Cooling type	TEFV
Silicon steel	35WW300
Angle of each channel, θ ($^\circ$)	22.5
Number of ventilation channels	16

Table 2 Controllable parameters and their levels

Factor	Parameter	1	2	3	4	5
A	n	6	7	8	9	10
B	h (mm)	13	14	15	–	–
C	th (mm)	1	2	3	–	–

n is the number of branches; th is the thickness of branches

specified as $35 \text{ m}^3/\text{min}$ by volume and 3500 Pa by pressure. With this volume rate of air coolant, the Reynolds number near the inlet is about 1.9×10^5 according to Eq. (1), which indicates the existence

of turbulent flow:

$$Re = \frac{\rho v d_\phi}{\mu} = \frac{4\rho Q}{\mu \pi d_\phi}, \quad (1)$$

where Re is the Reynolds number, ρ is the density of air, d_ϕ is the hydraulic diameter, v is the inlet velocity, μ is the kinematic viscosity, and Q is the volume-flow.

2.2 Overall lumped parameter and partial computational fluid dynamics model modeling

The zigzag plates were introduced to each channel to enhance convective heat transfer via larger contact area and turbulent intensity. The unique usage of zigzag plates combining with an annular cavity in the front end-cap led to a complex calculation of convective heat transfers inside channels and no analytical formulations could be found. Thus, the convective heat transfer in ventilation channels was discussed carefully based on a detailed LP model of each channel coupling with a partial 3D CFD model.

Taking the advantage of low-demand computing, an overall LP model of the motor was implemented and solved using the software Matlab for the zigzag plate design. Fig. 3 illustrates the overall LP model, and the detailed LP modeling of one ventilation channel, which describes the convective heat transfer from stator and housing to the air coolant as well as conductive heat transfer from stator to housing (Fig. 4). The abbreviations used in Figs. 3 and 4 are listed in Table 3. Copper losses P_{Cu} and iron losses P_{Fe} were evaluated using the software Maxwell, while mechanical losses were calculated by empirical formulations. The estimation values were 5.88 kW, 5.16 kW, and 4.20 kW, respectively. The iron losses consisted of stator loss 3.79 kW and rotor loss 1.37 kW. Because of the TEFV structure, friction losses of inner air and air coolant circulation were neglected. Analytical formulations from Wei et al. (1998), Wesseling (2001), and Micallef (2006) were used to model the convective heat transfers from the end-windings, shaft, and rotor to the end space. The initial convective heat transfers from the stator housing to the air coolant in channels were equivalent to parallel triangular ducts and modeled analytically (Bergman et al., 1990; Wei et al., 1998), while those precise transfers with zigzag plates for structure optimization were calculated using the coupled partial CFD model described in the following paragraph.

The thermal models of the remaining parts can be found in (Mellor et al., 1991; Boglietti et al., 2008, 2009; Chowdhury and Baski, 2010; Nategh et al., 2012).

The partial CFD model consisting of the front end-cap, ventilation channels, and air coolant domains was proposed in the environment of the software Fluent to simulate the turbulent flow condition and achieve convective coefficients. The $k-\epsilon$

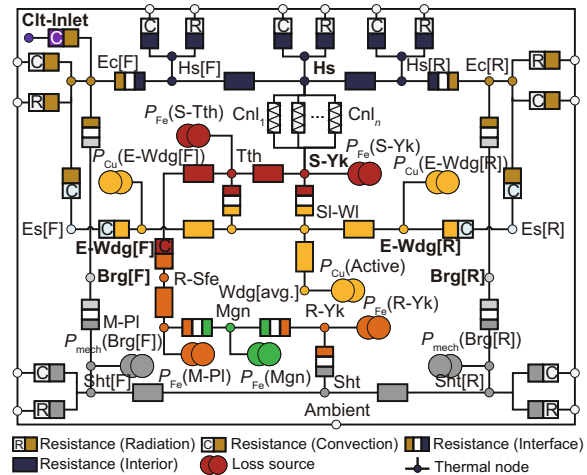


Fig. 3 Complete lumped parameter thermal model of the totally enclosed forced ventilation motor. Bold words represent temperature sensor locations in the experimental setup, and the abbreviations are listed in Table 3

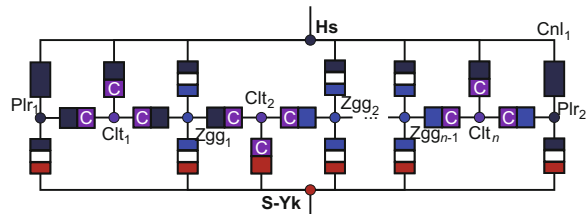


Fig. 4 Detailed lumped parameter model of heat transfers in ventilation channel 1. The abbreviations are listed in Table 3

Table 3 Abbreviations used in Figs. 3 and 4

Symbol	Description	Symbol	Description
[F]	Front	[R]	Rear
S-Yk	Stator yoke	R-Yk	Rotor yoke
Tth	Tooth	Hs	Housing
Ec	End-cap	Es	End space
Sl-Wl	Slot wall	Wdg	Winding
E-Wdg	End-winding	Mgn	Magnet
M-Pl	Magnet pole	Zgg	Zigzag plate
Brg	Bearing	Sht	Shaft
Clt	Coolant	Cnl	Channel
R-Sfe	Rotor surface	Plr	Pillar
P_{Cu}	Copper loss	P_{Fe}	Iron loss
P_{mech}	Mechanical loss		

re-normalization group (RNG) model was used in this CFD model (Shih et al., 1995). The Darcy-Weisbach equation was used for pressure drop and the Darcy friction factor was obtained from the Moody chart (Bergman et al., 1990). The CFD model was finely meshed and five boundary layers were applied for air coolant domains to discuss the boundary function. Fig. 5 shows an example of air coolant mesh. The convective coefficients, which were relevant to the air flow condition and heat flux in the ventilation channels, were calculated using the software ANSYS Fluent. The formulations for coefficient calculation are listed in Appendix A. Fig. 6 demonstrates the coupling progress of the LP and CFD models. First, ventilation convective heat transfers were initialized as parallel triangular

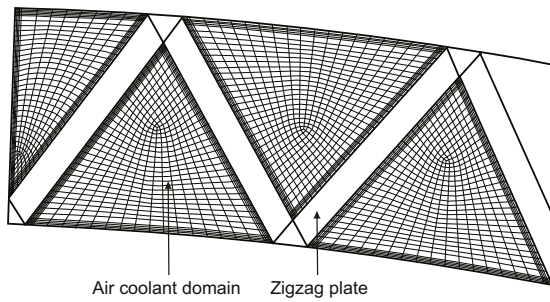


Fig. 5 Mesh of the air coolant area

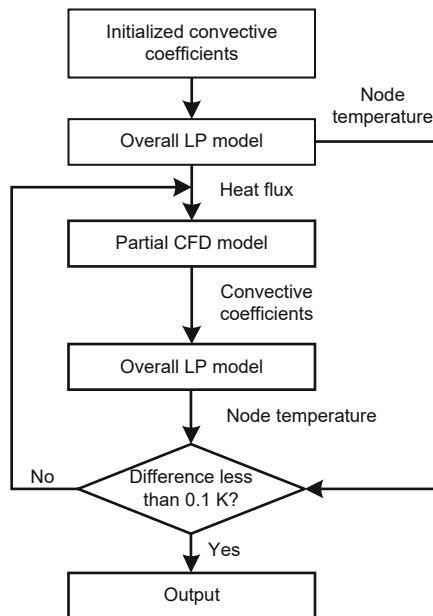


Fig. 6 Coupling progress of the overall lumped parameter model and the partial computational fluid dynamics model

ducts in the LP model. The results of initial temperature and heat flux from stator to coolant were then exported to the partial CFD model. Then the calculated convective coefficients attached to the air coolant were extracted to a data file and served as an input file for the LP model. Next, the newer results were again exported to the CFD model as a loop until errors of the last two calculation results in the LP model were less than 0.1 K.

2.3 Optimization results

To model all the 45 combinations according to the levels of critical parameters (Table 2), a massive computing effort could be involved. Therefore, Taguchi methods were implemented to obtain a feasible combination of design parameters (Taguchi et al., 2007). The Taguchi design ($L_{50}(6^1 \times 3^6)$) was adjusted to a simplified table of 15 cases by reducing the six-level factor into five-level and picking the first two three-level factors. Table 4 presents the results of pressure drop and temperature rises, where ΔP is the pressure drop from inlet to outlet, and T_{PM} and T_{end-w} are the temperature rises in PMs and end-windings, respectively.

Table 4 Data of parameter optimization

Case	n	h (mm)	th (mm)	ΔP (Pa)	T_{PM} (K)	T_{end-w} (K)
0	0	15	0	1640.80	140.74	182.45
1	6	13	1	2185.50	136.68	175.92
2	6	14	2	2237.08	134.24	173.08
3	6	15	3	2245.36	133.54	172.68
4	7	13	1	2307.96	130.52	169.23
5	7	14	2	2543.98	128.01	167.94
6	7	15	3	2517.48	127.68	165.14
7	8	13	2	3082.85	126.48	164.41
8	8	14	3	3166.64	125.68	163.45
9	8	15	1	2324.52	120.75	157.14
10	9	13	3	4094.44	128.41	168.47
11	9	14	1	2896.26	119.84	157.75
12	9	15	2	3014.65	118.14	156.34
13	10	13	2	3886.48	128.68	168.74
14	10	14	3	4647.95	117.45	156.89
15	10	15	1	3186.02	112.32	151.27

Case 0 is the original design without zigzag plates

Compared to the original design (case 0), the introduction of zigzag plates has improved thermal performance by decreasing temperature rises in both PMs and end-windings. By analyzing results of temperature rises under the same n value, it is clear that the thermal benefit from the increasing h value is

greater than that from the th value. Furthermore, the benefit from the increase of n value is greater than both h and th .

The effect of increasing the th value under the specific n and h values could be either positive or negative. Thicker branches make a contribution to conductive heat transfer by increasing conductive path areas and to turbulence intensity by decreasing air coolant areas. Meanwhile, the decrease of contact areas leads to an impressive influence on convective heat transfer. The effect of increasing the th value is the comprehensive result of conductive and convective changes. Therefore, the optimal combination for thermal performance should be the maximum n and h values with a reasonable th value, which is the situation for case 15 (Table 4).

By comparing the paired data of cases 2/3, 5/6, 7/8, and 11/12, it is found that thermal performance could barely gain or may even lose benefit from th . Prediction could be made that the combination of $n = 10$, $h = 15$, and $th = 2/3$ has a worse thermal performance compared to case 15. Furthermore, the pressure drop of combinations with $n > 10$ is clearly out of range according to the analysis of cases 12–14. Finally, critical parameters are determined as case 15. Compared to case 0 (the original design without zigzag plates), the thermal performance is improved by 20.19% and 17.09% for the magnets and the end-windings, respectively.

3 Complete 3D computational fluid dynamics model and experimental evaluation

3.1 Complete 3D computational fluid dynamics model

A complete 3D CFD model of the TEFV motor was implemented to obtain an accurate temperature distribution of key components. The important aspects of the CFD model are listed below:

1. The friction losses of rotation were neglected.
2. A 50-mm vertical virtual tube of air coolant before the inlet was built instead of the whole tube from wind source to inlet.
3. The end-windings were simplified as two annular cylinders.
4. An unstructured grid was used because of the complicated geometry of the motor (i.e. the air

coolant domain). On the walls of the air coolant, a number of layers of prismatic grid cells were used to obtain a more accurate wall function (Fig. 5).

5. The concentrated winding in the slots was simplified as tubes and wrapped with an insulating frame, and only insulation varnish (Li et al., 2010) was considered (Fig. 7).

6. The k - ϵ RNG model was used to evaluate the fluid dynamic and thermal behavior of the thermal equilibrium under a rated operation.

7. Standard wall functions were used in the case of turbulent flow.

Among all kinds of loss sources, the copper losses and iron losses were responsible for a large proportion and were considered carefully in the CFD model. Both kinds were pre-calculated by an electromagnetic model at the operating temperature T_0 predicted by the LP model in Section 2. Since the copper losses were dependent on the actual temperature of the windings, a user-defined function (UDF) file was compiled into the source term of copper zones according to the heat source calculation:

$$q = q_0 \cdot \frac{1 + a(T - T_{\text{ambient}})}{1 + a(T_0 - T_{\text{ambient}})}, \quad (2)$$

where q_0 is the volumetric heat source term at temperature T_0 , a is the temperature coefficient of copper, T is the actual volume-weighted temperature, and T_{ambient} is the ambient temperature.

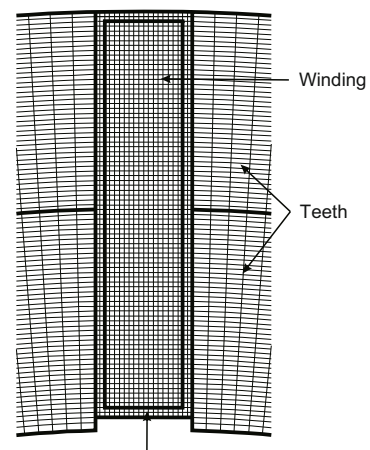


Fig. 7 Arrangement and mesh of winding insulation

As iron losses were relevant to the supply frequency as well as the magnetic flux densities, iron losses of the stator and the rotor were apportioned according to these values in respective regions (Mi

et al., 2003). Under a rated operation, the iron losses of the rotor were assumed to be uniform because of the interior structure type. Meanwhile, the flux density of the stator teeth varied dramatically in the radial direction and was very different from the yoke. On the basis of the flux density, the teeth domain was separated from the yoke and was divided equally into two parts (Fig. 8).

The thermal behavior of case 0 and case 15 solutions was evaluated under a rated operation with an ideal current supply and Fig. 9 shows the results of the key temperature distribution at an ambient of 303.15 K. Compared to the temperature limit of the insulation system (493.15 K), the temperature rises in the end-windings of case 0 and case 15 left

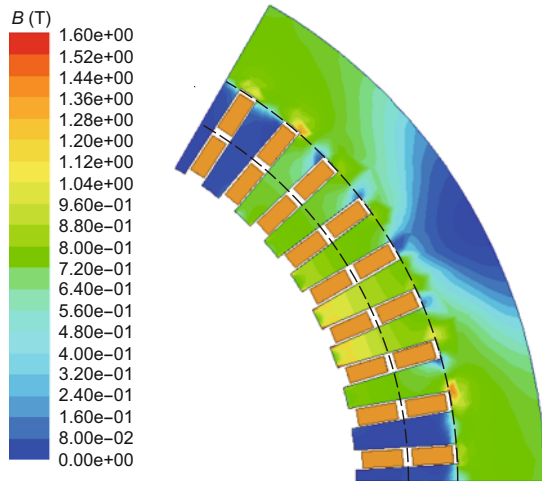


Fig. 8 Separation of the stator according to the magnetic flux density (B). References to color refer to the online version of this figure

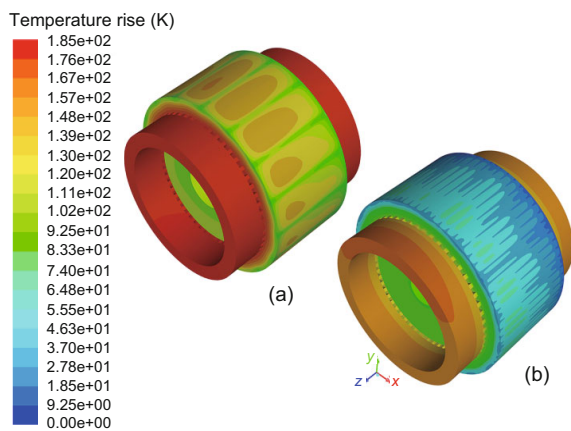


Fig. 9 Three-dimensional simulation results of temperature distribution of key components in motors: (a) case 0; (b) case 15. References to color refer to the online version of this figure

5.73 K and 31.37 K safety margin, respectively. For Sm30UH magnets (maximum operating temperature 573.15 K), the maximum temperature rises of case 0 and case 15 were far away from the limit. Although both solutions met the requirements of a normal operation, the temperature in the end-winding of case 0 was expected to exceed the limit of the insulation system because of the extra iron losses from harmonics with electronic devices.

3.2 Experimental evaluation

Tests were conducted by a twin drag system including the proposed PM motor and an induction motor at the same power level (Fig. 10). Under thermal equivalent operation, the rotor of the traction motor was driven to a rated speed by the induction motor while the stator was excited with sinusoidal currents at a rated value. Fig. 11 shows the mounting positions of thermocouples. Four thermocouples were circumferentially uniformly installed on both outer and inner layers of two end-windings, forming a temperature monitor net of 16 points. Four circular-distributed thermocouples were mounted in the middle of the stator. Data were sampled every



Fig. 10 Experimental setup of the twin drag system

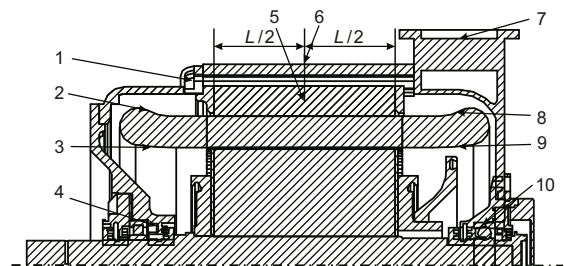


Fig. 11 Installation diagram of thermocouples. 1: air outlet; 2 and 8: outer layer of end-winding; 3 and 9: inner layer of end-winding; 4 and 10: bearing; 5: stator; 6: housing; 7: air inlet

minute until the temperature difference was less than 0.5 K within a 30-min interval and Fig. 12 shows the results.

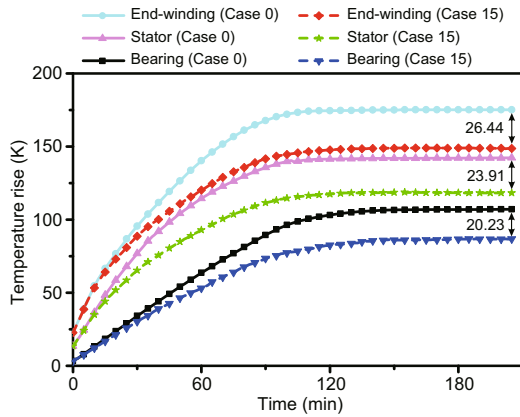


Fig. 12 Experimental results of temperature rises of key components in the totally enclosed forced ventilation motor under thermal equivalent operation with a rated current

Table 5 presents the results of case 0 and case 15 under thermal equivalent operation. The maximum values among the 16 points on end-windings and 2 points on bearings were marked respectively, while the temperature rises of the stator were evaluated by the average value. Assuming that the temperature change of the winding with natural cooling was linear after shutdown, the winding resistance, which varies linearly with the temperature of copper, was recorded for a period of time to estimate the operational winding temperature by linear fitting. According to the comparison (Table 5), both the proposed LP model and complete CFD model were verified by errors of less than 6%. Compared to case 0, the temperature rises of case 15 in the end-winding, stator, and bearing were decreased by 26.44 K (15.10%), 23.91 K (16.81%), and 20.23 K (18.91%), respectively. It can be seen that the ben-

efit of the optimized zigzag plates was greater than 15%.

4 Estimation of iron loss constraint

Through the thermal analysis by the CFD model, the maximum temperature rise points at the key components could be found and used to guide a more accurate and efficient online temperature monitoring (i.e. using fewer monitoring points). However, the temperature rises of rotational components were difficult to measure online. Using the validated CFD model, the maximum temperature rises of PMs could be estimated by analyzing the correlation between stator slots and PMs.

Although much work has been carried out on iron loss prediction in this kind of interior permanent magnet synchronous motor, there are still no precise methods to indicate iron losses with an inverter involved. In practice, the actual iron losses would increase because of time harmonics caused by semiconductor switching devices. Without considering the harmonic influence on iron losses, the results from the LP and CFD models could be rather different from the working temperature. The thermal behavior of the optimized motor driven by an inverter under the rated operation was evaluated by tests and Fig. 13 illustrates the results. The steady temperature rises of the end-winding, stator, and bearing were 181.65 K, 139.67 K, and 106.55 K, respectively. The influence of harmonics on iron losses led to an increase of 32.95 K for the end-windings. Assuming that the temperature difference between the end-windings and the PMs was the same as the thermal equivalent operation, the maximum temperature rise of the PMs was estimated to be 140.57 K. Given the material features of key components, the normal operation at the rated power was guaranteed

Table 5 Temperature rises and benefits of key components under thermal equivalent operation

	Component	End-winding	Winding	PM	Stator	Bearing
Case 0	LP (K)	182.45	176.07	140.74	150.65	108.32
	CFD (K)	181.43	173.28	138.82	148.33	108.54
	Measurement (K)	175.14	169.01	–	142.21	107.04
Case 15	LP (K)	151.27	142.12	112.32	122.62	90.53
	CFD (K)	153.86	145.96	111.25	121.45	88.96
	Measurement (K)	148.70	141.14	–	118.30	86.80
	Benefit (%)	15.10	16.49	–	16.81	18.91

and there is still some safety margin for severe working conditions.

An engineering method was proposed to estimate the iron loss constraint by assuming that extra harmonic iron losses in the stator yoke, stator teeth, and rotor were proportional to the volume-weighted average value of the flux density. Using the complete CFD model, temperature rises of end-windings and PMs under the rated current supply with different iron losses were evaluated and Fig. 14 shows the results. Both correlations between temperature rises and iron losses could be synthesized to a linear equation. From the results in Figs. 13 and 14, the iron loss under the rated traction operation was estimated to be 8.21 kW, while the measurement was 8.47 kW according to the standard IEC 60034 by the loss separation test method. The high coherence indicated that the proposed approach could be used

as a reference for the electro-magnetic and control system design.

5 Conclusions

Within the specification limit of the CRH380A bogie, zigzag plates were introduced to ventilation channels of a 600-kW TEFV PM traction motor and optimized using the overall LP model, in which detailed convective heat transfers were studied by the coupled partial CFD model. The temperature distribution of the motor was simulated using the complete 3D CFD model.

Both models were verified by experimental tests under the thermal equivalent operation with the rated current. The optimized ventilation structure ensures a normal operation of the traction motor as well as improving the thermal performance by more than 15%. This is of great significance for high-speed rail trains since the thermal performance of motors has been pushed to the limit. Additionally, an engineering method was proposed on the basis of the complete CFD model to estimate the iron loss constraint that can be used as a reference for the electro-magnetic and control system design.

The thermal analysis method using the overall LP with partial CFD modeling was proposed for cooling structure optimization of TEFV machines or water-cooling machines, in which the cooling structure can be extracted from the overall model for thermal coefficient calculation.

Future research will focus on iron loss modeling and a more specific thermal model of the rotor. Another research focus would be transient thermal evaluation of the traction motors under severe operations like frequent start and continuous climbing.

References

- Bergman TL, Incropera FP, DeWitt DP, et al., 1990. Fundamentals of Heat and Mass Transfer. John Wiley & Sons, USA.
- Boglietti A, Cavagnino A, 2007. Analysis of the endwinding cooling effects in TEFC induction motors. *IEEE Transactions on Industry Applications*, 43(5):1214-1222. <https://doi.org/10.1109/TIA.2007.904399>
- Boglietti A, Cavagnino A, Staton D, 2008. Determination of critical parameters in electrical machine thermal models. *IEEE Transactions on Industry Applications*, 44(4):1150-1159. <https://doi.org/10.1109/TIA.2008.926233>
- Boglietti A, Cavagnino A, Staton D, et al., 2009. Evolution and modern approaches for thermal analysis of electrical

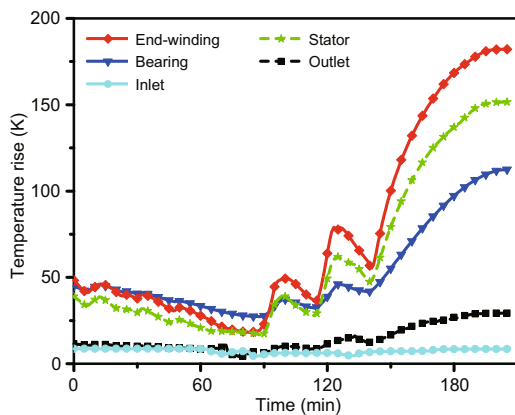


Fig. 13 Experimental results of temperature rises of key components in the totally enclosed forced ventilation motor driven with an inverter under the rated traction operation

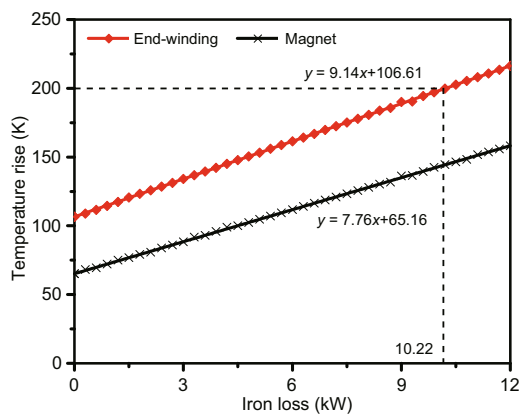


Fig. 14 Estimation of the correlations between temperature rises and iron losses under the rated current

- machines. *IEEE Transactions on Industrial Electronics*, 56(3):871-882.
<https://doi.org/10.1109/TIE.2008.2011622>
- Chowdhury SK, Baski PK, 2010. A simple lumped parameter thermal model for electrical machine of TEFC design. Joint International Conference on Power Electronics, Drives, and Energy Systems & Power India, p.1-7.
<https://doi.org/10.1109/PEDES.2010.5712385>
- El-Refaie AM, Jahns TM, McCleer PJ, et al., 2006. Experimental verification of optimal flux weakening in surface PM machines using concentrated windings. *IEEE Transactions on Industry Applications*, 42(2):443-453.
<https://doi.org/10.1109/TIA.2006.870043>
- Feng J, 2012. Development overview and application challenges of permanent magnet synchronous traction system for rail transit. *High Power Converter Technology*, 3:1-7 (in Chinese).
<https://doi.org/10.3969/j.issn.1671-8410-B.2012.03.003>
- Hao H, Fei WZ, Miao DM, et al., 2016. Torque characteristics in a large permanent magnet synchronous generator with stator radial ventilating air ducts. *Frontiers of Information Technology and Electronic Engineering*, 17(8):814-824.
<https://doi.org/10.1631/FITEE.1500238>
- He HB, Yao DW, Wu F, 2017. A reduced and optimized kinetic mechanism for coke oven gas as a clean alternative vehicle fuel. *Journal of Zhejiang University-SCIENCE A (Applied Physics & Engineering)*, 18(2):511-530.
<https://doi.org/10.1631/jzus.A1600636>
- Huang XY, Zhang JC, Sun CM, et al., 2015. A combined simulation of high speed train permanent magnet traction system using dynamic reluctance mesh model and Simulink. *Journal of Zhejiang University-SCIENCE A (Applied Physics & Engineering)*, 16(8):607-615.
<https://doi.org/10.1631/jzus.A1400284>
- Huang Y, Zhu J, Guo Y, 2009. Thermal analysis of high-speed SMC motor based on thermal network and 3-D FEA with rotational core loss included. *IEEE Transactions on Magnetics*, 45(10):4680-4683.
<https://doi.org/10.1109/TMAG.2009.2023065>
- Ji SM, Ge JQ, Tan DP, 2017. Wall contact effects of particle-wall collision process in a two-phase particle fluid. *Journal of Zhejiang University-SCIENCE A (Applied Physics & Engineering)*, 18(3):958-973.
<https://doi.org/10.1631/jzus.A1700039>
- Jungreuthmayer C, Bauml T, Winter O, et al., 2011. A detailed heat and fluid flow analysis of an internal permanent magnet synchronous machine by means of computational fluid dynamics. *IEEE Transactions on Industrial Electronics*, 59(12):4568-4578.
<https://doi.org/10.1109/TIE.2011.2176696>
- Kral C, Haumer A, Bauml T, 2008. Thermal model and behavior of a totally-enclosed-water-cooled squirrel-cage induction machine for traction applications. *IEEE Transactions on Industrial Electronics*, 55(10):3555-3565.
<https://doi.org/10.1109/TIE.2008.927242>
- Kral C, Haumer A, Haigis M, et al., 2009. Comparison of a CFD analysis and a thermal equivalent circuit model of a TEFC induction machine with measurements. *IEEE Transactions on Energy Conversion*, 24(4):809-818.
<https://doi.org/10.1109/TEC.2009.2025428>
- Li Q, Zhong J, Li Y, et al., 2010. Study on a C-class solvent-free silicone impregnating varnish. *IEEE Transactions on Dielectrics and Electrical Insulation*, 17(3):785-790.
<https://doi.org/10.1109/TDEI.2010.5492251>
- Mademlis C, Kioskeridis I, Margaris N, 2004. Optimal efficiency control strategy for interior permanent-magnet synchronous motor drives. *IEEE Transactions on Energy Conversion*, 19(4):715-723.
<https://doi.org/10.1109/TEC.2004.837282>
- Mellor PH, Roberts D, Turner DR, 1991. Lumped parameter thermal model for electrical machines of TEFC design. *IEE Proceedings B (Electric Power Applications)*, 138(5):205-218.
<https://doi.org/10.1049/ip-b.1991.0025>
- Mi C, Slemmon GR, Bonert R, 2003. Modeling of iron losses of permanent-magnet synchronous motors. *IEEE Transactions on Industry Applications*, 39(3):734-742.
<https://doi.org/10.1109/TIA.2003.810635>
- Micallef C, 2006. End Winding Cooling in Electric Machines. PhD Thesis, University of Nottingham, Nottingham, UK.
- Mizuno S, Noda S, Matsushita M, et al., 2013. Development of a totally enclosed fan-cooled traction motor. *IEEE Transactions on Industry Applications*, 49(4):1508-1514.
<https://doi.org/10.1109/TIA.2013.2256872>
- Nategh S, Wallmark O, Leksell M, et al., 2012. Thermal analysis of a PMaSRM using partial FEA and lumped parameter modeling. *IEEE Transactions on Energy Conversion*, 27(2):477-488.
<https://doi.org/10.1109/TEC.2012.2188295>
- Nategh S, Huang Z, Krings A, et al., 2013. Thermal modeling of directly cooled electric machines using lumped parameter and limited CFD analysis. *IEEE Transactions on Energy Conversion*, 28(4):979-990.
<https://doi.org/10.1109/TEC.2013.2283089>
- Qian JY, Liu BZ, Jin ZJ, et al., 2016. Numerical analysis of flow and cavitation characteristics in a pilot-control globe valve with different valve core displacements. *Journal of Zhejiang University-SCIENCE A (Applied Physics & Engineering)*, 17(5):54-64.
<https://doi.org/10.1631/jzus.A1500228>
- Shih TH, Liou WW, Shabbir A, et al., 1995. A new $k-\epsilon$ eddy viscosity model for high Reynolds number turbulent flows. *Computers & Fluids*, 24(3):227-238.
[https://doi.org/10.1016/0045-7930\(94\)00032-T](https://doi.org/10.1016/0045-7930(94)00032-T)
- Taguchi G, Chowdhury S, Wu Y, 2007. Introduction to orthogonal arrays. In: Taguchi's Quality Engineering Handbook. John Wiley & Sons, USA, p.584-596.
<https://doi.org/10.1002/9780470258354.ch35>
- Tan Z, Song XG, Ji B, et al., 2015. 3D thermal analysis of a permanent magnet motor with cooling fans. *Journal of Zhejiang University-SCIENCE A (Applied Physics & Engineering)*, 16(8):616-621.
<https://doi.org/10.1631/jzus.A1400293>
- Wei Y, Meng D, Wen J, 1998. Heat Transfer in Motors. China Machine Press, Beijing, China (in Chinese).
- Wesseling P, 2001. Principles of Computational Fluid Dynamics. Springer, New York, USA.

Appendix A: Calculation of convective coefficients

In the partial CFD model, the convective coefficients are calculated by

$$h_{\text{eff}} = \frac{\rho c_p u^*}{T_c^*} - \frac{D}{T_c^*(T_w - T_p)}, \quad (\text{A1})$$

where c_p is the specific heat, u^* is the near-wall turbulence velocity scale, D is the viscous heating, T_c^* is the dimensionless law-of-the-wall temperature, T_w is the temperature at wall, and T_p is the temperature at wall-adjacent cell centroid.

For standard wall treatment, the parameters T_c^* and D are modeled using the following composite forms:

$$T_c^* = \begin{cases} \text{Pr} y^*, & y^* \leq y_T^*, \\ \text{Pr}_t \left(\frac{1}{\kappa} \ln(E y^*) + P \right), & y^* > y_T^*, \end{cases} \quad (\text{A2})$$

$$D = \begin{cases} \frac{\rho u^*}{2} \text{Pr} U_P^2, & y^* \leq y_T^*, \\ \frac{\rho u^*}{2} (\text{Pr}_t U_P^2 + (\text{Pr} - \text{Pr}_t) U_c^2), & y^* > y_T^*, \end{cases} \quad (\text{A3})$$

where P is computed by

$$P = 9.24 \left(R^{3/4} - 1 \right) \left(1 + 0.28 \exp(-0.007R) \right), \quad (\text{A4})$$

with $R = \text{Pr}/\text{Pr}_t$ (Pr is the molecular Prandtl number and Pr_t is the turbulent Prandtl number), y^* is the dimensionless distance from wall, y_T^*

is the dimensionless thermal sublayer thickness, $\kappa = 0.4187$ is the von Kármán constant, $E = 9.793$ is the empirical constant, U_P is the velocity at wall-adjacent cell centroid, and U_c is the mean velocity magnitude at $y^* = y_T^*$.

中文概要

题目: 基于全局热网络和局部流体动力学建模的全封闭永磁牵引电机热性能优化

目的: 提出一种适用于全封闭冷却结构的电机热性能优化模型, 设计一台600 kW的高速列车用永磁牵引电机。

创新点: 1. 通过耦合局部流体动力学模型的方法求解电机复杂冷却风道内的对流传热系数, 并在全局热网络模型的框架内得到快速、准确的电机温升结果以用于结构优化; 2. 在冷却风道中引入栅格结构, 采用热性能分析模型优化冷却结构, 提升电机热性能; 3. 通过三维流体动力学模型计算电机局部温升最大值, 并提出一种预测特定结构下电机铁损工作阈值的工程方法。

方法: 1. 采用热网络法建立全局热网络模型(图3), 并通过耦合局部流体动力学模型计算风道内的热网络参数(图4和6); 2. 应用田口设计法对电机风道结构进行优化, 并研制样机进行验证(计算与试验结果见表5); 3. 假设铁损的谐波附加值与磁密值成正比, 通过三维流体动力学模型计算给出端部绕组、永磁体温升值与铁损的预测曲线, 并用样机试验进行验证。

结论: 1. 采用全局热网络和局部流体动力学建模的方法可以快速、正确地计算复杂冷却结构下的电机温升分布, 且优化后的冷却结构至少可以提升文中电机15%的热性能; 2. 本文提出的优化模型适用于全封闭风冷或者水冷等冷却结构相对独立且尚无经验公式可参考的电机热性能优化设计; 3. 铁损工作阈值的预测方法可以为电磁和控制系统设计提供参考。

关键词: 热网络模型; 流体动力学; 永磁电机; 全封闭强制风冷